SCIENCE ROBOTICS | RESEARCH ARTICLE

BIOMIMETICS

From grasping to manipulation with gecko-inspired adhesives on a multifinger gripper

Wilson Ruotolo*, Dane Brouwer, Mark R. Cutkosky

Anthropomorphic robotic manipulators have high grasp mobility and task flexibility but struggle to match the practical strength of parallel jaw grippers. Gecko-inspired adhesives are a promising technology to span that gap in performance, but three key principles must be maintained for their efficient usage: high contact area, shear load sharing, and evenly distributed normal stress. This work presents an anthropomorphic end effector that combines those adhesive principles with the mobility and stiffness of a multiphalange, multifinger design. Adhesive suspensions use buckling ribs to deliver shear load sharing and normal compliance in a deployable form factor. We use an elastic foundation model and fundamentals of grasping theory to motivate kinematic changes when shifting from Coulomb friction to adhesive manipulation. These design considerations integrate with the necessary control infrastructure in a prototype called farmHand, on which we perform tests to confirm shear load sharing and demonstrate adhesive use in manipulation beyond pick and place grasping.

INTRODUCTION

Anthropomorphic hands have existed in research circles for more than 30 years, yet simple parallel grippers continue to be the norm in manufacturing and real-world applications because they deliver strong grips in a light and compact package (*1*, *2*). Many-jointed hands have major kinematic advantages over their less mobile counterparts but must also deliver robust, powerful functionality comparable with that of a parallel jaw gripper if they are to be adopted in more practical settings.

Gecko-inspired adhesives can help achieve grasping strength through the use of van der Waals forces (*3*–*5*). Originally used for climbing applications where the objective is to sustain shear loads (parallel to the surface) under negative normal forces (away from the surface) (*6*–*10*), dry adhesives can also improve the gripping capability of hands while reducing the size of required actuators (*11*, *12*). However, gecko-inspired adhesive gripper designs to date generally focus on low-torque applications such as grasping in space (*13*) or applications like pick-and-place operations where the gravity load is primarily in a single direction (*14*, *15*). Some grippers have begun including gecko-inspired adhesives on their grasping surfaces, but the designs that exploit astrictive [i.e., with negative normal pressure (*16*)] contact conditions efficiently have resulted in grasps that cannot manipulate. These past explorations characterize both the high potential and the diverse implementation difficulties seen with adhesives.

Some designs focus on even load sharing between contact patches at the cost of contact area or grasp selection. It has been shown that the maximum sustainable shear stress in both natural and engineered adhesives decreases with the scale of the pad (*10*). Therefore, when seeking to exert substantial forces, one must split the contact into multiple small patches and then load those patches such that each experiences the same shear stress across its adhesive area. Previously, this shear load distribution has been accomplished with differential pulley mechanisms (*13*) or by using the degressive stiffness of superelastic elements (*10*). These implementations, however, rely on contact with flat or gently curved surfaces and are not intended to accommodate variations in object shape where the radius of curvature may be less than the length of the gripper.

Other designs focus on achieving high contact area at the cost of load sharing efficiency. Soft, pneumatically actuated grippers are capable of matching adhesive surfaces to an impressive array of shapes (*12*, *17*, *18*), but the use of highly compliant materials for many or all components of the hand limits the ability to controllably reorient objects due to insufficient grasp stiffness. In addition, adhesive films actuated over compliant, ribbed skeletons have been used to achieve shear loading while conforming to curved shapes without peeling (*19*, *20*), but these grippers do not conform to small, irregular objects or withstand substantial side loads. Further, neither the pneumatic grippers nor the film grippers have mechanisms to evenly distribute irregular shear loads that arise during use.

In summary, although several compliant mechanisms and hands have been developed to exploit adhesion, none of these support general manipulation: accommodating a wide range of objects and allowing the robot to control their position and orientation while applying forces and moments in arbitrary directions. This work extends gecko-inspired adhesives from primarily unidirectional grasping to general manipulation with multifingered hands (Fig. 1). The extension rests upon the combination of a strong, selectively stiff multiphalangeal hand with three adhesive principles: high contact area, shear load sharing between contact patches, and even normal stress on a given contact patch. If a given gripper-object contact patch is simplified to a single plane, then shear loads are those parallel with this plane (Fig. 2, x direction) and normal loads are orthogonal to it (Fig. 2, y direction). Shear load sharing is accomplished using diagonal buckling beam structures that display degressive shear stiffness at the object-finger interfaces, a solution that can be deployed on any adhesive equipped gripper. Degressive stiffness, as the term is used in (*10*), refers to a flat zone in the force-displacement curve where, for some interval, increased displacement induces minimal additional spring force. Large real area of contact and evenly distributed normal stresses on contact patches are achieved by joint configurations and torque distributions that center contact patches on the phalange faces, conditions that are different from the ideal configurations for Coulomb friction only.

Department of Mechanical Engineering, Stanford University, 424 Panama Mall, Stanford, CA 94305, USA.
*Corresponding author. Email: wruotolo@stanford.edu

Fig. 1. Manipulator introduction. (Left to right) farmHand demonstrates its gentle, hyperextended pinch on a raw egg, a high-force power grasp on a pumpkin, and a low–wrap angle manipulation of an object much larger than the gripper itself.

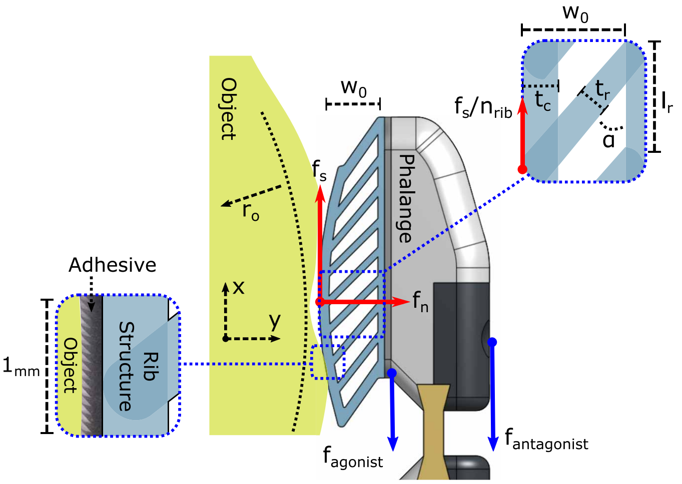

Fig. 2. Buckling rib parameters. Diagram of angled elastic rib pad, with forces and geometric parameters labeled. f_s and f_n are the shear and normal force, respectively, exerted by the object on the phalange. Right inset shows the parameters of a single rib, which can be altered to tune the stress-strain properties of the structure; the left inset shows a zoomed-in view detailing the relative size and orientation of the adhesive. The recommended design order of these parameters with their associated constraints is tabulated in the Supplementary Materials.

The adhesives used for testing consist of a directional, microwedge design as presented in (*21*)—but our purpose is to address the hand design considerations necessary for efficient use of any directional adhesive, independent of the material properties and force limits of that particular implementation. The adhesives selected for our experiments are chosen for their high shear force capacity, but other adhesives could be used for different performance priorities such as higher temperature fluctuations or wet environments.

We combine the three design principles of manipulation with adhesive contact (contact area, shear load sharing, and evenly distributed normal stress) in a semi-anthropomorphic prototype. Originally designed for gentle manipulation of fruit as a robotic farming aid and because it was created at Stanford, otherwise known as "The Farm," we call this end effector farmHand. As a general manipulator that is also capable of efficiently using dry adhesive technology, this prototype can forcefully manipulate heavy objects many times its own size yet maintains the gentle dexterity to pluck eggs from a carton and grapes from the vine (Fig. 1 and movie S1).

RESULTS

Local compliance and global load sharing

Shear load sharing is a key principle of adhesive manipulation, but it must be accomplished while also maintaining high total contact area. Compliance perpendicular to a surface promotes conformation for nonflat or misaligned surfaces. Compliance in the shear direction can promote load sharing if it has a nonlinear softening or degressive characteristic so that different contact patches that undergo different displacements experience approximately the same shear force (*10*). The need to combine degressive stiffness in shear with compliance in the normal direction is why it does not suffice to back adhesives with a uniform, isotropic material (e.g., a soft foam) or prior hierarchical structures such as in (*7*).

Figure 2 shows a passive, ribbed structure that provides a nearly constant shear force for a range of shear deflections while also providing normal compliance. Unlike nitinol-based solutions for flat surfaces (*10*), tiles with differentials (*6*, *22*, *23*), or other previous load sharing mechanisms (*13*, *24*), this solution can be applied to any manipulation system regardless of actuation scheme or manipulator geometry—for example, a parallel jaw gripper, a multifingered robotic or prosthetic hand, or even an exoskeleton. A local *xy* coordinate system is aligned tangential and perpendicular to the contact surface, nominally at the center of pressure. We assume that the *x* axis points in the distal direction along a phalange or gripper and *y* is orthogonal to the finger pad. A single-rib structure is illustrated in Fig. 2. On a given phalange of farmHand, four of these pads are arranged in parallel. A three-dimensional (3D) model is provided in Materials and Methods.

As the object is displaced under loading in the *x* direction, bending of the ribs results in decreasing stiffness to shear loads (deformation pattern shown in movie S2 and Fig. 3A). If we denote the shear force by f_s, the desired degressive elastic behavior is characterized by $df_s/dx \approx 0$ for a desirable range of displacements and associated loads. Too large of a positive df_s/dx value leads to traditional spring mechanics that have no load sharing effect because the ribs will not sufficiently soften to accommodate multiple displacements at the same force value. Conversely, df_s/dx going too negative results in jumps in displacement under constant or slightly increasing shear force (as would occur when an object is being picked up) due to the decrease in force, f_s, associated with increasing displacement, dx. A negative stiffness results in a pseudo-bistable condition that is undesirable for controlled manipulation. The desired plateau in load/displacement behavior is most important at moderate and high loads to prevent premature failure of any contact patch that makes contact before its neighbors. At the same time, it should occur at some safety margin below the maximum shear force, $f_{s_{max}}$, that the adhesive can sustain. Examples of these conditions are provided in Fig. 3.

The stress-strain performance of the rib design is described by the rib angle, α; rib thickness, t_r; top surface thickness, t_c; pad height, w_0; and spacing between ribs, l_r (illustrated in Fig. 2), along with material properties. The effects of varying these parameters are interrelated, but the following design sequence reduces coupling and the need for iteration.

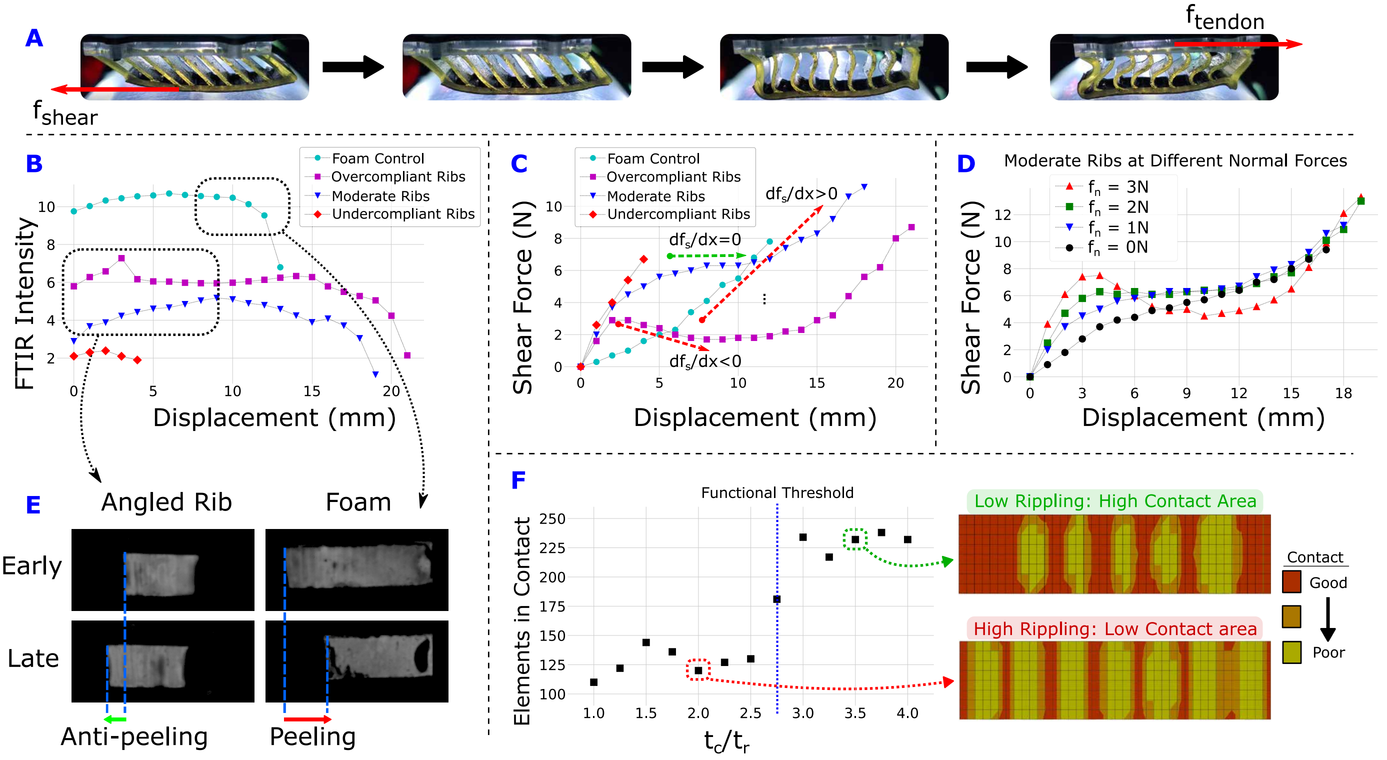

Fig. 3. Testing and analysis of individual angled rib structures. (**A**) An overcompliant angled rib pad undergoes shear loading, demonstrating the stages of buckling. (**B**) Real area of contact, as determined by FTIR, plotted against shear displacement for three angled rib structures and a foam pad sample. FTIR intensity is reported in average grayscale intensity per pixel. Although the soft foam structure achieves high peak contact area, the degressive structures maintain contact area under load, explaining higher shear load capability as seen in (C). (**C**) Shear force versus displacement plots of the same structures, demonstrating overcompliant, undercompliant, and moderately compliant degressive plateaus. (**D**) Force versus displacement plots of the moderate angled rib structure with varying normal force, showing changes in degressive plateau shape. (**E**) FTIR images of contact area propagation under load, illustrating the anti-peeling properties of farmHand's ribbed pads. (**F**) ANSYS simulation results plotting contact area versus the relative thickness of the contacting surface. An increase in rippling suppression is seen above $t_c/t_r \approx 2.75$. Simulation snapshots before and after this cutoff show a structure able to achieve substantial contact area (red) and one which is more inhibited by rippling at the contacting surface.

Decreasing rib thickness, t_r, and top surface thickness, t_c, promotes conformation to nonflat surfaces. t_r should be minimized within fabrication limits. If t_c/t_r is too small, however, the upper surface will ripple under load and decrease contact area. Finite element analysis indicates that a functional threshold for elastomeric materials is about $t_c/t_r > 2.75$ (Fig. 3F, see Materials and Methods for details). Therefore, t_c is set according to this ratio after t_r has been minimized.

Increasing w_0 reduces stiffness and provides the structure with increased travel in the normal direction to conform to surfaces. However, it also makes the structure bulky and increases the moment produced by the offset in the y direction between the surface tangential force, f_s, and the reaction force in the substrate. The desired w_0 value thus depends on the expected object curvature, parameterized by r_o, and should be chosen to match the sagitta of the arc defined by the object radius and the length of the phalange, l_x (depicted as s in fig. S1). We extend this analysis to a range of r_o values in text S3.

Decreasing α causes the degressive plateau to occur earlier, decreases stiffness in the normal direction, and increases stiffness in shear; α is thus reduced until there is a region for which $df_s/dx \approx 0$. The influence of α will vary by normal force (Fig. 3D). Smaller l_r results in higher rib density and thus stiffer bulk properties. Overcompliance results in premature structural failure before using the full adhesive capacity, whereas undercompliance decreases contact area, leading to an adhesive failure at lower force values. Thus, the density of the ribs is maximized subject to the constraint that the shear force plateau, f_p, still occurs below $f_{s_{\max}}$. This design order and its associated constraints are collected in table S1.

Figure 3 presents testing data showing the behavior of undercompliant, overcompliant, and moderately compliant rib prototypes, with a foam rubber pad of comparable stiffness for comparison. Materials and Methods provides testing details, and fig. S2 presents the test setup. The soft and moderate variants exhibit a plateau region for which the shear force is nearly constant with increasing shear load and corresponding displacement. The softest variant exhibits a range for which $df_s/dx < 0$, which is undesirable, as noted above. The stiffest variant does not conform enough to achieve a large contact area and thus fails in shear before reaching its plateau. The moderate rib structure shows a desirable flat plateau in shear force for normal forces between 1 and 2 N, corresponding to pressures of 2.5 to 5.0 kPa over the 40 mm–by–10 mm surface (Fig. 3D). The plateau shear force, f_p, of 6 N is safely below $f_{s_{\max}} \approx 10$ N.

Anti-peeling

The diagonal ribs improve single-pad performance in addition to the multipad benefit of load sharing presented above. Under shear load in the preferential direction, these anisotropic structures initially displace toward the grasped object rather than away from it as would be expected with a linear-elastic pad. This behavior increases contact area and normal pressure at the trailing edge where most adhesive failures begin, thus improving peak shear force capacity.

Contact patch evolution is measured during stress-strain trials using a custom-built frustrated total internal reflection (FTIR) test setup. FTIR is a method of assessing contact at the micrometer scale (*25*). Figure 3 (B and E) shows the resulting area measurements, which indicate that premature drop-off in contact area is a stronger predictor of adhesive performance than peak contact area. In the case of the linear-elastic control, the trailing edge of the contact patch peels away from the surface (Fig. 3E), leading to decreased maximum pull-off force (Fig. 3B). In contrast, the asymmetric stiffness of the ribbed structures passively prevents peeling by displacing toward the object when being pulled in shear and thereby pushing the trailing edge farther into contact (Fig. 3E). This effect is a function of the rib geometry, not the adhesive-surface interface, and so will occur whenever the ribs are loaded in the preferential direction. These results are echoed later as a secondary artifact of load sharing testing in the "Load sharing validation" section.

Single-phalange kinematics

Finger kinematics, grasp theory, and actuation schemes are integral components of any manipulation system and are well studied in traditional Coulombic regimes (*26*–*28*), but different considerations must be made under astrictive contact conditions (*16*, *22*). Contact area and shear load sharing remain paramount, although we now assume that the rib structures provide these functions. Adhesive surfaces strictly improve shear force capacity and affect normal forces minimally; thus, Coulomb friction–based metrics of grasp integrity as they exist in the literature serve as a conservative starting point (*29*, *30*). In addition, surface normals beneficial to Coulombic grasps also aid adhesive grasps; thus, much of the recent planning literature, e.g., (*31*), remains relevant. As such, we focus our kinematic adaptations on conditions when traditional grasps do not excel: high forces aligned with the shear components of the contact wrench and high torques at a single contact patch. These conditions are prevalent when grasping and manipulating planar objects; convex objects where the characteristic radius, r_o, is substantially larger than the length of a phalange; and small objects for which occlusion or interference prevents an enveloping grasp.

Essentially, we seek to choose and adapt the grasp configuration so as to maximize the intimate contact area while also meeting task-dependent constraints. However, maximizing real contact area is a difficult control objective to use directly because it is hard to measure, and it is not obvious how to adjust a grasp toward better contact even with good data. Instead, we introduce and control $\overrightarrow{c_p}$, a vector from the center of the phalange face to the center of pressure of the contact patch in the *xz* plane. The magnitude and direction of this value are comparatively easy to control through actuation and measure with modern tactile sensors. For efficient adhesive usage, the magnitude of $\overrightarrow{c_p}$ should be minimized to increase both the contact area and uniformity of the pressure distribution (the combination of which results in high shear force capacity as discussed below). We investigate the implications of $\overrightarrow{c_p}$ on shear force capacity for a single phalange and then extend that analysis to full-hand pullout force in key configurations. These analyses form a framework on which to base adhesive contact equipped finger control. In addition, although increasing the magnitude of $\overrightarrow{c_p}$ results in a monotonic decrease in maximum shear force capacity of a given pad, there are three zones determining the magnitude of this effect that should be considered when designing task constraints.

Prior art involving gecko-inspired adhesives predominantly focuses on characterization of the limit curve for negative normal forces (*32*–*34*). Those that have included positive normal forces typically simplify that sector of the limit curve to a linear approximation (*35*), which is reasonable with stiff adhesive substrates. Conversely, it was shown in (*11*) that when adhesives are backed with compliant structures, there is a nonlinear decrease in effective friction coefficient with increasing normal force

$$\tau_{\max} = a_1 \sigma^{a_2} + \tau_0 \tag{1}$$

where σ, $\tau_{\max}$, and τ_0 represent the normal stress, maximum sustainable shear stress, and sustainable shear stress with zero normal force, respectively, for a given element of the contact patch, and constants a_1 and a_2 are empirically determined for each adhesive, compliant suspension, and object material. This relationship will approach a linear coefficient of friction at high normal stresses or almost immediately for rough objects with little adhesion (*3*). Data used to generate this curve for our rib structures are shown in Fig. 4A. Acrylic, brushed steel, and paper were chosen as common materials representative of low, medium, and high absolute rugosity, respectively. It has been shown that, rather than surface polarity or charge, this metric of roughness primarily determines the strength of the van der Waals forces due to its influence on achievable intimate contact area (*36*, *37*).

Although originally applied to civil engineering, Winkler elastic foundations have also been used to model soft matter adhesive phenomena (*38*, *39*). Adapting such a model to the prototype rib structures, we can predict an elemental normal foundation stress, $\sigma_{(x,z)}$, as a function of local strain, $\epsilon_{(x,z)}$ (subscripts omitted henceforth for simplicity of notation), by fitting a third-order polynomial function to capture both the initial degression due to buckling effects and the later progressive inflection point due to inter-rib contact (Fig. 4B and Eq. 2). This result is then combined with adhesive performance through Eq. 1 to estimate the theoretical maximum shear force of an adhesive equipped pad for a given contact

$$\sigma = b_1\epsilon^3 + b_2\epsilon^2 + b_3\epsilon \tag{2}$$

$$f_{s_{\max}} = \int_A \left(a_1 \left(b_1\epsilon^3 + b_2\epsilon^2 + b_3\epsilon \right)^{a_2} + \tau_0 \right) dA \tag{3}$$

where b_1, b_2, and b_3 are curve fit parameters for the degressive to progressive normal stiffness of the structures and ϵ is the strain seen by a given element of the compliant pad. ϵ is a function of grasped object geometry and its penetration into the pad. Equation 3 is used to plot the shear performance of the adhesives versus $\overrightarrow{c_p}$ for planar surfaces of varying normal force (Fig. 4C) and convex surfaces of varying characteristic radius (Fig. 4D). $\overrightarrow{c_p}$ is only shown varying in the *x* direction, but the same analysis applies for *z*-direction components.

If the rib structure's stiffness properties are changed through new geometry or material selection, then the experimental characterization presented in Fig. 4B would need to be performed again. If the adhesive, surface, or immediate adhesive substrate (e.g., the top layer of the rib structure) were changed, new data would need to be collected similarly to Fig. 4A. Any of these changes will alter the numerical inputs to the model presented here, and thus the quantitative

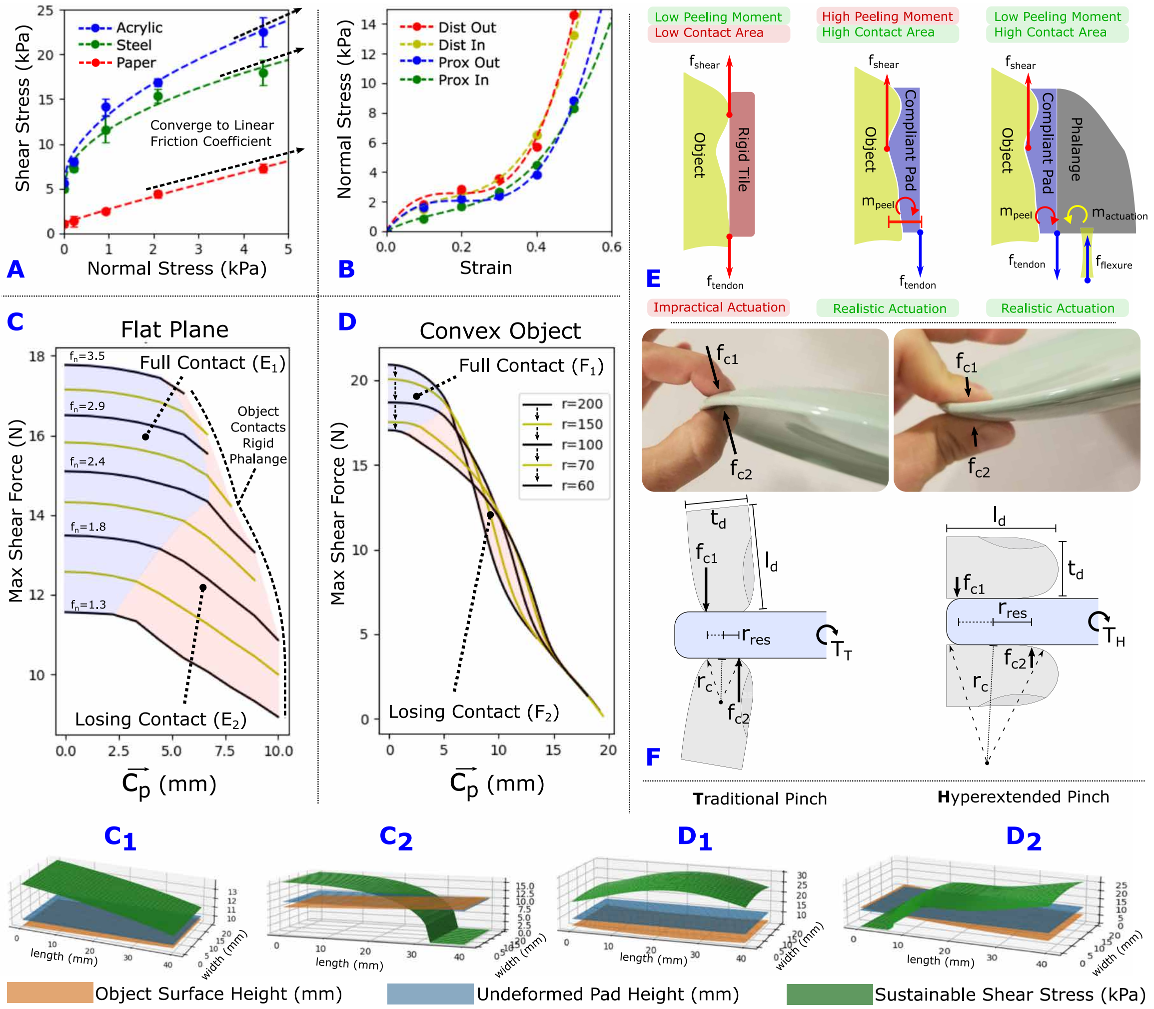

Fig. 4. Effects of single-phalange kinematics. (**A**) Sustainable shear stress versus normal stress of one adhesive isolated from the degressive ribs. Each data point is an average of five trials, with error bars representing one sample SD. Acrylic and brushed steel both display substantial adhesion, but paper is almost completely defined by Coulomb friction. (**B**) Data points and curve fit (according to Eq. 2) for compressive normal stress versus strain of each of the four rib suspension sizes. (**C**) Simulation results showing shear force capacity as $\vec{c}_p$ varies for a single 40 mm–by–20 mm pad (discretized into 1-mm^2 elements) in contact with a flat plane of acrylic. Variations in $\vec{c}_p$ are achieved by changing the contact angle about the *z* axis. Snapshots (C_1) and (C_2) show the object penetrating into the pad along with resultant sustainable shear stress for each contacted element. These are respectively characteristic of the first two zones of diminishing adhesive performance. (**D**) Simulation results for spherical acrylic of varying radii. Peak penetration is held constant while the object is virtually rolled across the surface, resulting in changing $\vec{c}_p$. Snapshots of the first two zones of adhesive performance loss are provided below (D_1 and D_2). (**E**) Planar characterization of adhesive rolling and peeling challenges when actuated against an irregular object with compliant suspension. (**F**) Critical dimensions for torque output analysis of a distally hyperextended pinch versus a traditional pinch. f_c, r_{res}, and r_c represent the contact force during pinching, resultant moment arm, and effective radius of curvature, respectively. T_H and T_T are the torque applicable in the hyperextended and traditional pinch cases.

results, but the procedure remains constant. In addition, the resultant trends that are discussed below will hold true for minor changes in stiffness properties but could change if different adhesives are used or fundamental structural properties are altered (such as switching from a degressively stiff to a progressively stiff design). Potential work with other adhesives is explored in Discussion.

Universally, higher $\vec{c}_p$ results in a lower $f_{s_{\max}}$; thus, minimization of $\vec{c}_p$ is critical to high single-pad performance. For small deviations in $\vec{c}_p$ (zone 1; Fig. 4, C and D, blue), the reductions in maximum shear force stem only from uneven normal stress distribution (Fig. 4, C_1 and D_1). The losses result from the nonlinear nature of the limit curve, which favors conditions with f_n spread evenly across all adhesive elements rather than concentrated on a smaller subset of the contact. As $\vec{c}_p$ increases into zone 2 (Fig. 4, C and D, red), edges of the pad begin to lose contact, which results in more pronounced shear capacity losses (Fig. 4, C_2 and D_2). Last, if $\vec{c}_p$ reaches beyond the border of the pad itself, this results in a bulk peeling moment (Fig. 4E) that is beyond the torque-balancing capacity of the phalange, analogous to the support boundary–based stability criteria of mobile bases (*40*, *41*). This third zone of $\vec{c}_p$ results in an immediate and catastrophic rolling failure of the entire structure and must be avoided for successful manipulation.

Thus, a kinematic objective of any manipulation seeking to efficiently use compliantly backed adhesive surfaces is to minimize the magnitude of $\vec{c}_p$ at each contact patch while allowing the normal and shear forces to contribute to the overall force balance. This may require changing the phalange orientation as the grasp complies in response to changes in loading. In this manner, local pad performance is determined by global kinematic behavior, whereas global load sharing performance is achieved through local mechanical properties. The goal of minimizing $\vec{c_p}$ is explored below for pinch grasps and enveloping grasps to illustrate grasp configuration differences between Coulombic and adhesive conditions.

Power pinch kinematics

At least two degrees of freedom are needed to allow fingers to achieve both power wraps and precision pinches, so farmHand implements two phalanges per finger. Single-finger control is consequently divided into two schemes based on whether only the distal phalange is in contact (typically the case in pinch grasps) or both phalanges are in contact (typically seen in enveloping grasps) (*42*). We first address the former.

An advantage that parallel jaw grippers have over their more anthropomorphic, multiphalangeal counterparts is the potential for high grasp force and hence a high pullout force using a single precise mechanism. Conversely, the fingertip pinch achieved by many multifingered hands delivers small surface areas of contact at the end of a set of phalanges where the maximum forces for a given actuator torque are low. farmHand overcomes this limitation with its adhesive pinch grasps, which can be viewed as an adhesive extension of some of the advantages noted for frictional hyperextended pinch grasps in (*43*, *44*).

Adhesive pinches should use the front face of the finger rather than the tip because this presents more available contact area (Fig. 4F). Contact area and $\vec{c_p}$ do not affect a grasp relying on Coulomb friction; the maximum shear force, $f_{s_{\max}} = \mu f_n$, depends on the joint torque distribution that maximizes f_n. Conversely, the adhesive pinch is more sensitive to $\vec{c_p}$ than f_n, so the ideal joint torque distribution shifts to decrease f_n in favor of more contact area and a uniform normal stress.

To explore the trade-off, we adapt a two-link Jacobian to the scenario by removing the constraint that the final link length is fixed, similar to free-ended analyses used for whole-arm manipulation (*45*). We assume the center of pressure rolls along the finger face to a variable distance that is a function of the ratio of proximal to distal torque. The details of this treatment are presented in text S1, and the resulting relationship is

$$c_{px} = \frac{T_d l_p \cos\theta_p}{(T_p - T_d)\cos(\theta_p + \theta_d)} - l_d/2 \tag{4}$$

where T_p and θ_p and T_d and θ_d are the proximal and distal joint torques and angles, respectively, and l_d is the distal phalange length (see Fig. 5). The motors used in farmHand deliver about 0.5 Nm of available torque at the proximal joint in most configurations. Figure 5 plots the computed pullout force in the *x* direction from a single finger with this torque available in the Coulomb friction case (Fig. 5B) and the adhesive case (Fig. 5C) for a range of $\vec{c_p}$ spanning the half length of the distal phalange (±25% of l_d or 20 mm of the 40-mm length of the prototype hand). We also note that for the same joint torques and with ideal loading geometry, the maximum pullout force is several times higher with adhesion than with Coulomb friction (Fig. 5C).

Figure 5 (B and C) illustrates several key trends. Pullout force in the Coulombic case increases linearly with decreasing T_d, resulting in the highest pullout force when the lever arm from the proximal joint to the center of pressure of the normal force is shortest (Fig. 5B2). In the adhesive case, however, the local maximum in pullout force for a given T_p occurs at the T_d value, resulting in a centered normal force on the face of the phalange and thus $\vec{c_p} \approx 0$ (Fig. 5C). The height of this peak varies based on adhesive strength, but the trend remains evident whenever the maximum adhesive shear force, $f_{s_{\max}}$, is substantially larger than μf_n.

To extend this unidirectional analysis of shear capacity to a multi-axis limit curve, one can superpose a negative term representing the loss of performance due to non-ideal loading angle on the results shown in Fig. 5. This method is verified in the discussion section of (*11*). Normal pressure and contact area distributions are functions of geometry and normal compliance, so they, along with the Coulomb friction results, are unaffected by loading direction.

Power pinch torque output

The above considerations address optimization of adhesive pinching for the f_x, f_z, and m_y components of the contact wrench, whereas f_y is controlled directly via the actuators. However, the shift from finger tip to finger face also improves the ability to exert moments m_x and m_z about the contact patch. In grasp theory, it is common to capture this effect with a wrench selection matrix, H, that represents which of the six force and moment components are transmitted through a contact (*46*, *47*). For a small contact patch, H typically has rank 3, and for a soft contact, rank 4, to transmit moments, m_y. When required to exert higher torques, a human will default to the hyperextended configuration shown in Fig. 4F, resulting in the "very soft finger" model with H of rank 6 (*48*). Designing manipulators to capitalize on such a selection matrix is uncommon, but effective (*43*, *44*, *49*, *50*). If we continuously control the orientation to minimize $\vec{c_p}$, then, by definition, m_z will be small for volitional actions. However, the passive response of the contact to perturbations will still benefit from a large contact patch that can sustain moments m_x and m_z.

These two wrench components are both torques modeled as a function of normal force ($\vec{f_c} = [f_{c1}, f_{c2}]$) acting on a resultant moment arm (r_{res} in Fig. 4F), and thus, the maximum applicable torque for a given normal force is linearly improved by increasing that distance. Most biological and robotic systems have longer characteristic length than thickness of a given phalange, and Fig. 4F shows $l_d \approx 2 \cdot t_d$, resulting in 2× the applicable torque if the finger is simply rotated to the face (rather than the tip) before contact

$$\frac{T_{H_{\max}}}{T_{T_{\max}}} = \frac{l_d}{t_d} \cdot \frac{\|\vec{f_c}\|_{H_{\max}}}{\|\vec{f_c}\|_{T_{\max}}} \tag{5}$$

Here, $\|\vec{f_c}\|_{T_{\max}}$ and $\|\vec{f_c}\|_{H_{\max}}$ are the maximum normal force applicable by the traditional and hyperextended pinches, respectively, and l_d and t_d are the length and thickness, respectively, of the distal phalange as shown in Fig. 4F.

There is also a kinematic benefit of having a nearly flat contact. It arises from the motion of the contact coordinate frame as a function of rolling. The movement of the coordinate frame for a small change in grasp configuration (e.g., due to a change in external load) can be computed as a function of the relative curvature of the contact, which depends on both the fingertip and the object: $r_e = (1/r_{\text{fing}} + 1/r_{\text{obj}})$. A convenient metric of the stabilizing effect of contact rolling is the grasp stiffness matrix (*51*)

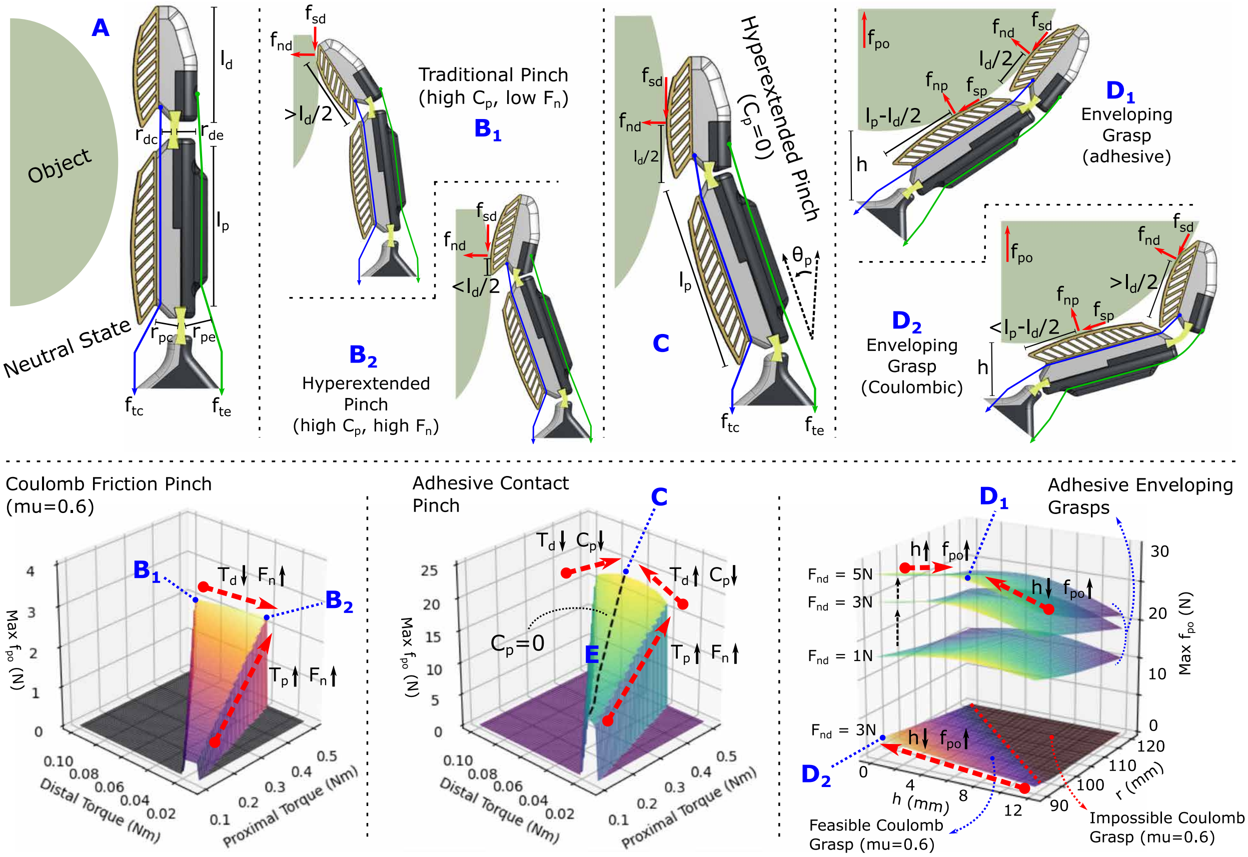

Fig. 5. Effects of joint configuration. (**A**) One finger in its neutral state with key dimensions labeled. Offset of flexure joint locations is implemented intentionally to allow for two tendon control of distal hyperextension. (**B**) A traditional fingertip pinch, often used in anthropomorphic hands and resulting in relatively low normal force and low stability, is contrasted against the maximum normal force configuration available for a given proximal joint torque. The latter would correspond to the best pullout force with Coulomb friction. Below, the maximum pullout force, f_{po}, is explored in simulation as proximal and distal torques vary (μ = 0.6). Configurations (B_1) and (B_2) demonstrate that in the case of Coulomb friction, pullout force is maximized by increasing proximal torque but decreasing distal torque (trends of increasing f_{po} are shown in red). (**C**) The finger is shown in a hyperextended pinch, with the center of pressure located at the midpoint of the distal phalange. Below, simulation results show adhesive pullout force for a feasible range of joint torques for the farmHand prototype. Although this condition reduces the maximum normal force for a given joint torque, it results in the largest value of f_{po} due to improved adhesive utilization. (**D**) Multicontact, enveloping grasp scenarios are examined for an idealized spherical object. The pullout force with Coulomb friction is maximized by minimizing h, the distance from the palm to the object, whereas the adhesive optimum is achieved at an intermediate h value that balances contact quality with desirable force directions.

$$K_e = K_b + K_j = \left({}^{P}_{B}J^{T}\right)\frac{\delta f_f}{\delta x_b} + \frac{\delta\left({}^{P}_{B}J^{T}\right) f_f}{\delta x_b} \qquad (6)$$

where ${}^{P}_{B}J^{T}$ is the transpose of the transformation matrix that maps small motions of the object to corresponding motions of the contact, f_f is the contact wrench, and δx_b is a perturbation of the object. The first term, K_b, represents the direct contribution of the finger stiffness, which is a function of joint servoing and structural stiffness. The second term, K_j, represents the effects of small changes in the grasp configuration. For point contacts, this term may be destabilizing, but for large r_e, it is usually stabilizing (positive definite). The kinematic effect of increasing r_e accounts for why holding a sphere between the thumb and index finger is more stable than holding a coin of the same diameter on edge (*48*).

For the case of a two-phalange, opposed finger system pinching a block with rolling contacts of radius r_c, Cutkosky and Kao (*51*) show two conditions derived from their equation 31 that are needed to maintain a positive definite K_e matrix:

$$\|\vec{f_c}\|/2 < r_c k_a \qquad \|\vec{f_c}\|/2 < \left(\frac{r_c k_c}{r_c + 1}\right)\left(\frac{k_b}{k_b + k_c}\right) \qquad (7)$$

where f_c is the normal force applied by the fingers and the k values shown are constant joint stiffnesses independent of grasp configuration. Thus, the maximum allowable normal force before instability occurs is linearly related to the radius of curvature at the point of contact, and the resulting increase in allowable normal force can be substituted back into Eq. 5 to show a quadratic relationship between maximum applicable torque of a pinch grasp and the size of the contact patch

$$\frac{\|\vec{f_c}\|_{H_{\max}}}{\|\vec{f_c}\|_{T_{\max}}} = \frac{l_d}{t_d} \qquad \frac{T_{H_{\max}}}{T_{T_{\max}}} = \left(\frac{l_d}{t_d}\right)^2 \qquad (8)$$

farmHand implements its hyperextended pinch by adding an independently controlled antagonistic tendon with offset flexure joints (Fig. 5A) for a total of two tendons per finger. This design allows direct control of the hyperextended pinch orientation at any position of the finger by holding the curling tendon at constant length while decreasing the length of the extending tendon. Further, allowing the extensor tendon to run free while actuating the curling tendon results in a curling of the finger into an enveloping grasp (Fig. 5D) where a second contact is made with the object. Text S4 discusses the position control algorithm, and text S2 maps desired contact forces to controllable tendon tensions.

Enveloping grasp kinematics

With a second contact patch on the same finger, we use geometrical constraints to solve directly for joint configuration and contact location using a bottom-up approach starting at the proximal phalange (*22*). With joint configuration known, finger contact forces are projected along the direction orthogonal to the palm as an assessment of f_{po}, pullout force capacity

$$f_{po} = \left[\sin\theta_p \;\; \cos\theta_p \;\; \sin(\theta_p + \theta_d) \;\; \cos(\theta_p + \theta_d)\right] \begin{bmatrix} f_{np} \\ f_{sp} \\ f_{nd} \\ f_{sd} \end{bmatrix} \tag{9}$$

Limit curves are shown in Fig. 5D across a range of h (the distance from base of object to palm) and r (object radius). Proximal normal force is held at a constant unit value, whereas distal force varies from 1 to 5 N in the adhesive case and is shown at 3 N for the Coulombic case.

Figure 5D communicates several key points pertaining to grasp configuration. The Coulombic case is monotonically affected by both parameters (r and h), whereas the adhesive performance reaches a local maximum for a given object radius at an h value corresponding to reduced $\vec{c_p}$ magnitudes. The resultant difference in grasp configuration is shown in Fig. 5 (D_1 and D_2). The latter shows the classical Coulombic intuition to press the object into the palm to maximize the component of f_{sd} projected away from the hand (as a human would do to palm a basketball). Figure $5D_1$, however, shows that adhesive performance is improved when the grasp is relaxed, h is extended slightly, and both contact patches are more centered on their respective phalanges.

Load sharing validation

The contact patch with degressive stiffness, along with the kinematic control considerations just described, was tested in a Robot Operating System (ROS)–based infrastructure (see Materials and Methods and text S4). Validation focused on load sharing and manipulation testing. After mounting the hand to a Universal Robots UR5 collaborative robot arm, a simple pattern (Algorithm 1) was used to apply controlled offsets between phalanges while measuring the resulting shear force on a sensorized linear rail system. The offsets simulate in a controlled way what would typically occur if the hand were misaligned as it closed on an object, or if an uneven force were applied to the object. Figure 6 shows the hand in the middle of a lifting task with an offset between two fingers. The corresponding data for the degressive rib structures and a foam control sample are plotted beneath for low, medium, and large offsets.

```
Algorithm 1 Testing procedure for controlled displacements.
1: Position hand in opposed pinch pre-grasp
2: Engage phalange one (Fig. 6A)
3: Apply displacement one by raising UR5 arm
4: Engage phalange two (Fig. 6B)
5: Apply displacement two by raising UR5 arm further
```

The ribs substantially reduce the difference in maximum shear stress experienced by the two phalanges, allowing the grasps to sustain higher total lifting forces, especially for the large offset case. There is a visible drop-off in the foam control data where the test overloaded the force capacity of the first phalange before the second could engage, causing the first phalange to slip. There is no slippage in any of the degressive data. In addition, the rib-backed adhesives consistently sustained 8 N of force in the plateau region, whereas the foam structures began slipping at 6 N despite contacting with the same area. We hypothesize that the difference stems from the anti-peeling advantages associated with inclined ribs that cause the surface to move outward while deforming in shear.

Manipulation performance

Manipulation testing assessed hand performance while grasping a range of objects and moving them with a UR5 arm in patterns that subjected them to forces and moments in 6 degrees of freedom. Movie S1 provides a demonstration of such manipulations. Figure 7 shows snapshots of grasps and manipulation sequences that characterize the design principles discussed. In the first column, farmHand performs grasps that can be difficult for anthropomorphic manipulators without adhesion, especially if we consider the ability for a single hand to perform all four grasps shown. In the second column, we show corresponding manipulation tasks for similar grasps, but with forces and moments in a variety of directions.

Figure 7 (A and B) shows two different uses of the pinch grasp: exploiting adhesion to extract an egg from a carton and exploiting a large contact area to sustain large moments while grasping the edge of plate. At the medium scale, Fig. 7C shows the ability to envelop soft and fragile objects (a cluster of grapes), whereas Fig. 7D shows variable grasp selection via simultaneous grips of a single grape and an apple. An enveloping wrap grasp (Fig. 7E) allows the robot to hold a powered angle grinder in a secure grip, which is juxtaposed with an image of in-hand manipulation (Fig. 7F) that exploits having multiple actuated tendons per finger. Figure 7G shows grasping of a large and slippery plastic bin using adhesion, whereas Fig. 7H demonstrates manipulation of a 3-kg container of orange juice. We believe that no previously reported robotic hand is equally capable of all these manipulations.

DISCUSSION

Gecko-inspired adhesives are a promising technology for grasping and manipulation, but their utility has been limited by the strict loading principles required to use them efficiently. Load sharing has been addressed in specific applications, but with restrictions on external loading that preclude general manipulation with a wide range of objects. We present a combination of principles that allow adhesives to be used on multifingered hands for general-purpose grasping and manipulation of a wide range of object geometries and sizes and for general manipulation with arbitrary orientations.

In summary, the principles are (i) degressive compliant finger pads that provide large contact areas while also providing global shear load sharing and preventing peeling from uneven pressure distributions and (ii) a control strategy that keeps phalange orientations aligned to local surface normals to reduce uneven pressure distributions.

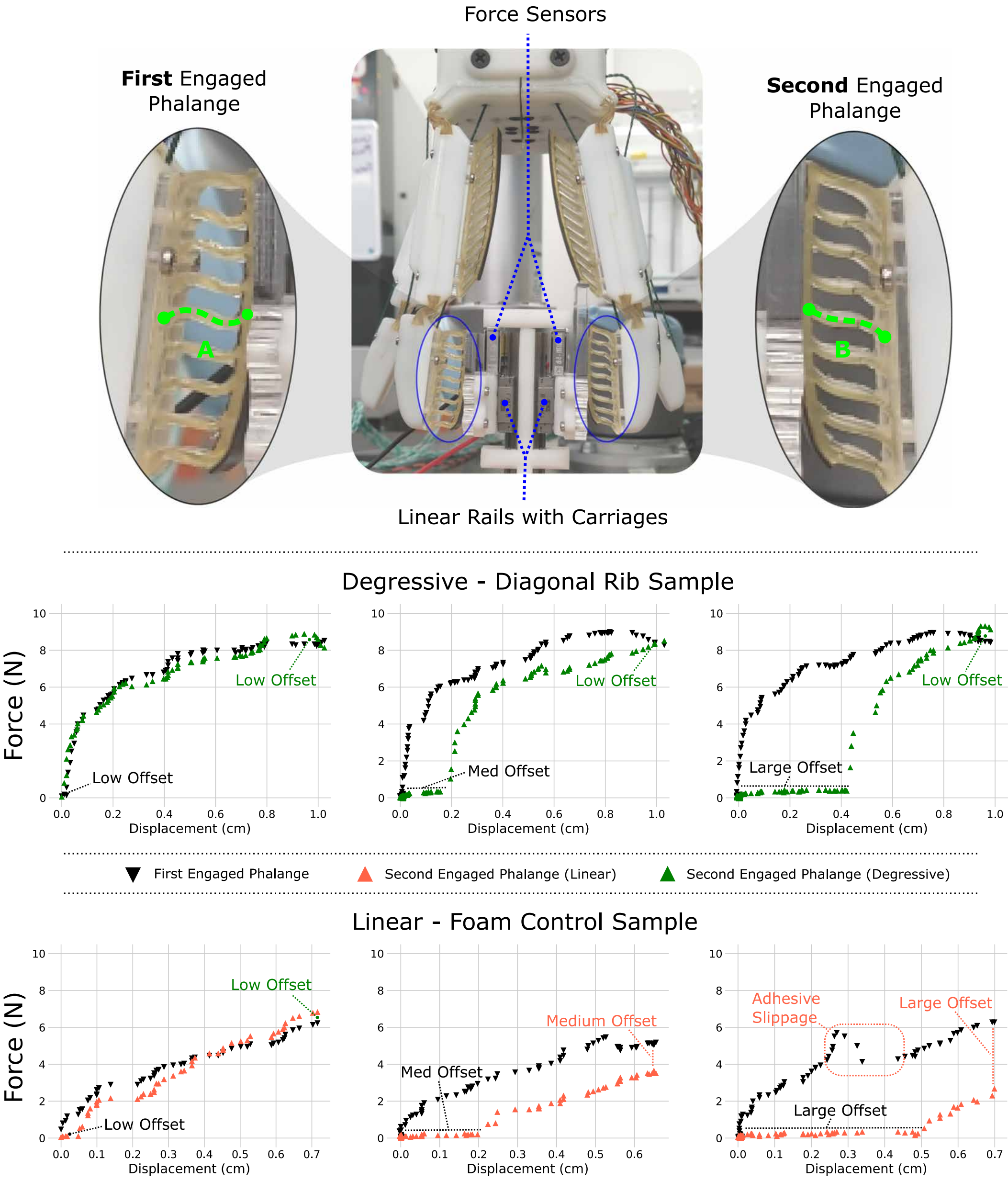

Fig. 6. Load sharing testing. Top: Frame capture from load sharing testing videos and plots of associated testing data. Phalange A was engaged first, an offset applied, and then phalange B was engaged before final loading. This resulted in notably more degressive buckling in the ribs on A than those on B, but no substantial difference in shear force. One row of plots shows results using degressive rib structures at three different offset values, and a second row shows the same tests run using a nondegressive, foam-backed control. The degressive structures show substantially less difference in shear force on the two phalanges than the foam in all cases where an initial displacement offset is present.

We implement the principles in an under-actuated, four-digit hand that uses adhesives to obtain substantially better maximum load performance than would be available with Coulomb friction and can achieve a variety of pinch and wrap grasps on large and small objects.

Tests show that the degressive force/deflection property of angled ribs on the finger pads provides both load sharing and conformation to surfaces. Multifinger tests also show that the proposed design and control scheme distributes loads evenly, with shear forces converging to an upper bound for the pads despite initial uneven loading or misalignment. These results are not unique to the two-phalange pinch grasp used in testing, because the same effect occurs regardless of which two (or more) rib structures are in contact. Thus, load sharing is achieved between multiple pads on the same phalange, multiple phalanges on the same finger, and across all four fingers and eight phalanges at once. There is no hypothetical limit to the deployable number and locations of the load sharing mechanism.

To enhance the performance across multiple phalanges and digits, we implement a control scheme that attempts to minimize nonuniformity in the pressure distribution at each contact. This scheme is in contrast to traditional schemes for underactuated hands that seek to maintain a uniform normal force across all contacts (*52*) and to schemes that attempt to optimize combinations of normal and friction forces for maximum pullout force (*53*–*55*).

The performance of the hand shows that general-purpose manipulation with gecko-inspired adhesives is practical, delivering both grasp strength and mobility in a single device. Thus, farmHand helps bridge the gap between the practicality of parallel jaw grippers and the flexibility of anthropomorphic hands.

The low cost of the first farmHand prototype leaves several opportunities for component upgrades. Higher motor torque would allow for higher tendon tension and therefore stiffer ribs, stiffer grasps, and higher overall stability. In addition, higher-quality sensing of the flexure bending [e.g., as in (*56*)] would improve control and could provide out-of-plane proprioception. In addition, direct measurement of tendon tension would eliminate a need for recalibration between tests.

The current farmHand prototype used the same adhesive and the same rib design (though scaled based on phalange size) for all of its

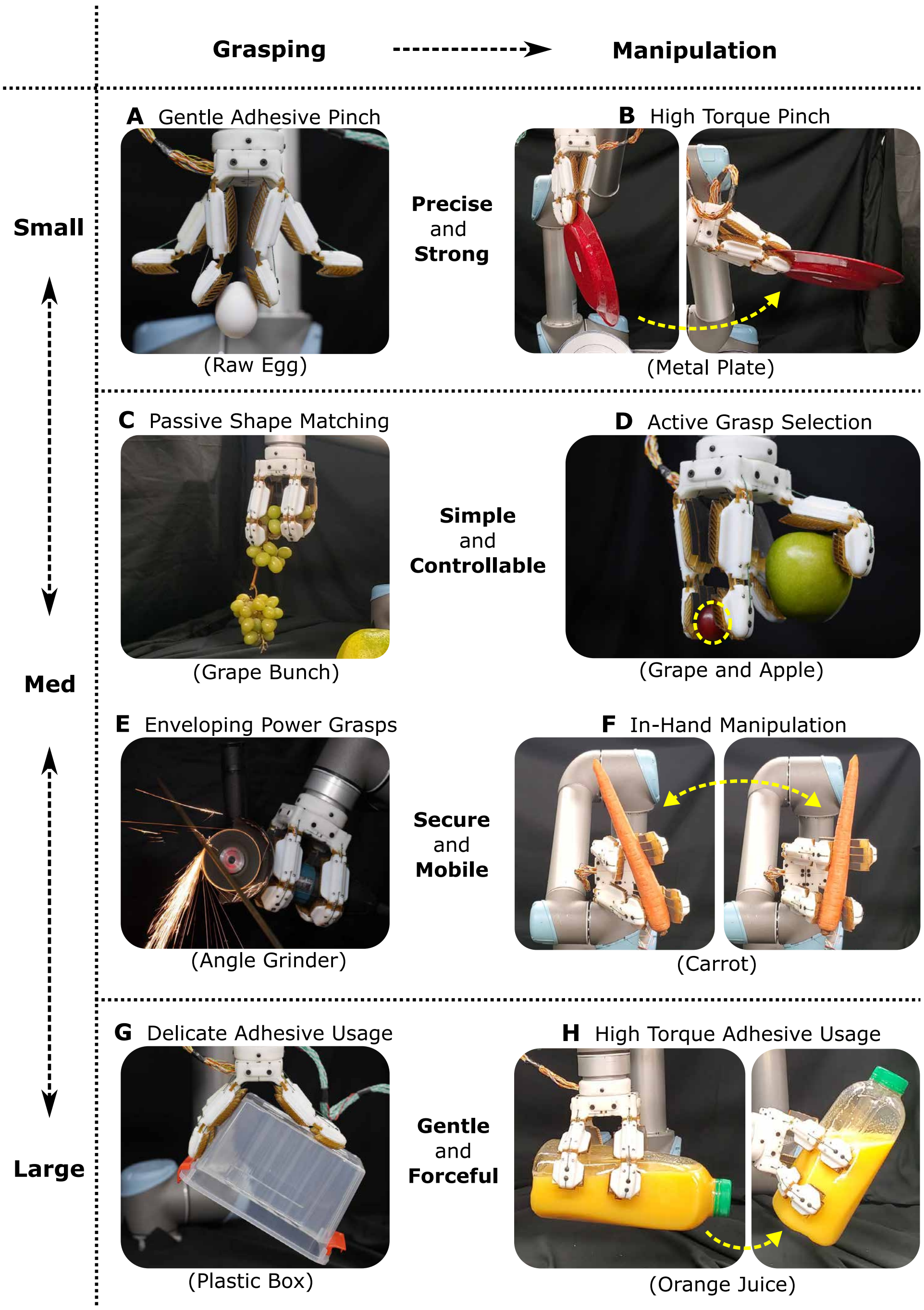

Fig. 7. Manipulation testing. (**A**) An egg is pinched on only the exposed top edge, showing an exaggerated example of the hyperextended pinch grasp and its utility in an adhesive regime. (**B**) A heavy plate is pinched and rotated with only the distal phalanges, showing the increased torque capacity of the hyperextended pinch. (**C**) An irregular bunch of grapes is grasped with an underactuated enveloping maneuver. (**D**) A grape and apple are grasped together, demonstrating independent control of the fingers. (**E**) An angle grinder is grasped with sufficient stiffness for secure operation. (**F**) In-hand manipulation is demonstrated by reorienting a carrot in a double-pinch grip. (**G**) A large box is grasped with low wrap angle, demonstrating the adhesive performance. (**H**) A heavy orange juice container is grabbed and rotated at high torque, relying on degressive buckling for load sharing.

primary contact patches. This homogeneous solution has general utility, but there remain opportunities to specialize portions of the hand with adhesive designs. In particular, one could vary the stiffness of ribs expected to encounter higher or lower forces or rotate a subset of ribs to better accommodate lateral loads or areas of high localized torque. In addition, many of the desirable effects that stem from the rib design could also be achieved with diagonal pillars or other such geometries capable of buckling in a range of shear angles, which permits a wide range of potential optimization. Further, the current rib design is particularly well suited for use with directional adhesives, because aligning the preferential directions of each leads to high shear performance, but the same principles of degressive load sharing, high contact area, and evenly distributed normal stress will still benefit a nondirectional adhesive. As such, one could extend the design concepts presented here to a wider range of environments and tasks by changing some, or all, of the adhesives to a new modality such as the underwater solution presented in (*57*) or the low-temperature results in (*58*).

A final, particularly interesting body of work is to include tactile sensing at the object gripper interface. Such an addition would enable an entire body of research concerning active control of the contact patches and loading of the hand. Most tactile servoing is performed with a focus on normal forces and high-level decision making (*59*, *60*), and often, shear forces and normal stress distributions are neglected. There are thus many opportunities to adapt existing grasp selection and control theory to a new set of constraints and performance metrics, such as dynamically adapting grasp configurations based on changing contact area to use the adhesives more efficiently. The deformation of the compliant rib structures provides opportunities for sensing using piezoresistive, magnetic, capacitive, or optical transducers.

MATERIALS AND METHODS

Testing

Single-pad testing was performed using the test rig shown in fig. S2A. An anchor point allowed for different pads to be mounted, and a linear rail allowed for vertical height adjustment. An adjustable spring suspension system was used to counteract the weight of the rail system, so the additional weights dictate the entirety of the functional normal force applied. A ball-bearing carriage and guide rail allowed for motion in the shear direction. Various normal forces were imposed by placing calibrated weights on the top of this rail to emulate varying grasp forces. Once weighted, shear displacement was imposed in increments of 1 mm, and the shear force was recorded using a digital force gauge (Mark-10, model M4-50, 0.1-N resolution) while corresponding snapshots of the evolving contact patch were captured at each increment. The same Mark-10 force gauge was used to measure shear force and normal force during the trials shown in Fig. 4, A and B, respectively, whereas normal stresses were applied via calibrated weights for Fig. 4A, and displacement was applied through 1-mm stepping of a Grizzly G8689 mini mill for Fig. 4B. Except where noted in the caption for Fig. 4A, all other data plotted are individual values and each curve plotted is a single trial of a sequential collection process.

Contact area was measured using FTIR (*11*, *33*) on an acrylic semicylinder (12.7 cm diameter). Light-emitting diodes (LEDs) illuminated the acrylic surface from the side in a blacked-out room. Because of the acrylic's high index of refraction, this light was internally reflected until an object, such as the silicone of our adhesives, contacted the outer surface.

A 170° fisheye lens universal serial bus (USB) camera with 1920 pixel–by–1080 pixel resolution was used to view and record the resulting light pattern. The postprocessing steps for contact area assessment are shown in fig. S2C. Before each trial, a grayscale calibration image was taken, which only captures illumination due to defects in the acrylic. The raw images were first converted to grayscale. Next, the initial calibration frame was subtracted from the grayscale images. To remove artifacts resulting from illumination of the sides of the pads or linear rail as displacement is imposed, a binary threshold was implemented. The FTIR intensity was then reported as the sum of all remaining pixel values normalized by the total number of pixels.

For two-phalange load sharing testing, the same smaller linear rail was used on both sides of a vertical support beam shown in Fig. 6. Two acrylic blocks were mounted on these guide rails via ball-bearing carriages. Single-axis force sensors (Futek, model LSB200, 5 lb, JR S-Beam Load Cell) were mounted as a stopper for the carriages. The farmHand prototype, equipped with only one pad per phalange, was commanded to grip the two blocks in a multistep process that allowed for application of controlled offsets between the two phalanges. The ROS infrastructure was built to simultaneously sample the two force measurements from the force sensors and the position of the UR5 wrist as a measurement of real, rather than commanded, offset.

Rib structures

Rib structures were fabricated using 3D-printed molds and cast urethane (Fig. 8). Molds were printed on a StataSys Objet24 3D printer, and Smooth-On PMC-780 was selected as the rib material for its strength and stiffness in the desired range (6.2 MPa tensile strength, 750% elongation at break, 80A shore hardness, and 2.8 MPa 100% modulus). This material is not the only effective option, because one could compensate for stiffer materials with thinner ribs or larger rib spacing and vice versa. The 3D printer provided ±0.1 mm control over rib thicknesses in our molds, but the viscosity of the liquid PMC-780 limited us to feature sizes of 0.5 mm and above. Upon assembly, the molds were coated with Smooth-On Universal Mold Release to allow for easy removal of the thin geometries being cast. Microwedge gecko-inspired adhesives as manufactured in (*61*) were adhered to the outer surface of the pads using a combination of Loctite Instant Adhesive and double-stick tape.

ANSYS model setup and testing

Simulated contact area as a function of (t_c/t_r) was conducted in an ANSYS Structural analysis by importing geometries with minimum possible rib thickness according to our manufacturing method (0.5 mm). These geometries were simplified to reduce stochasticity and improve solver convergence. A parameter was then created to sweep the thickness of the contacting surface from 0.5 to 2 mm in increments of 0.25 mm. For each design point, a fixed constraint was applied to the base of the pad structure, and a controlled compression of 1 mm was imposed on the pad by a flat rigid object. The

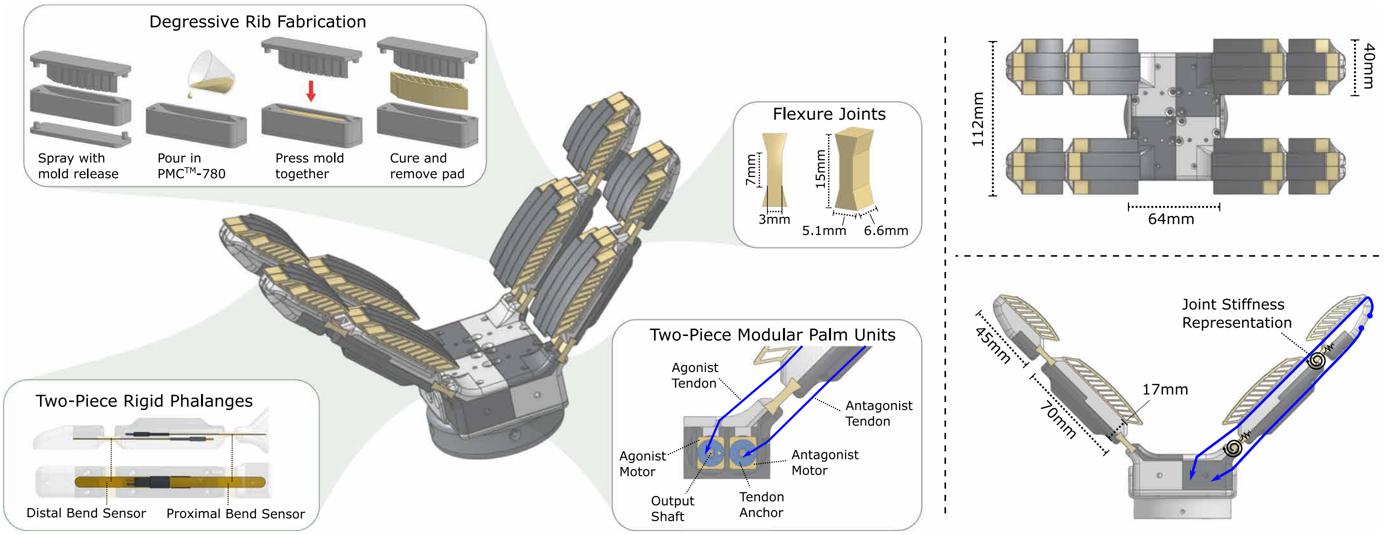

Fig. 8. Mechanical design and rib fabrication. Computer-aided design (CAD) renderings of the hand are provided from isometric, top, and side angles with exploded views of key features. Major dimensions are labeled in the top and side views along with a kinematic representation of the tendon system and compliant flexure joints. The hand consists of four independent modular palm/finger segments that are able to function independently and can be rearranged as needed. Each proximal phalange houses two bend sensors for proprioception at the proximal and distal joint. The angled rib structure fabrication process is also explained in four simplified steps.

contacting meshes were defined with a pinball radius (sphere of influence) of 0.1 mm and friction coefficient, $\mu = 10$, to approximate the relevant dimensions (adhesive wedge height is 100 μm) and contact conditions of the adhesives. A two-parameter Mooney-Rivlin material model using coefficients $C_{10} = 0.74$ MPa and $C_{01} = 0.1$ MPa was used to replicate the 100% modulus ($E_{100} = 2.76$ MPa) and hyperelastic behavior of PMC-780. A status plot under the contact results node was generated to categorize mesh elements as far, near, sliding, or sticking. This status plot was exported and postprocessed to count the elements in contact as defined by sliding or sticking.

Hand and fingers

Four identical fingers were chosen as a compromise between diversity of grasp options and complexity of fabrication. Figure 8 shows external dimensions and internal placement of tendons and sensors. Tendons were routed according to the hyperextension concepts described in the kinematics sections above. Each finger was actuated with two motors that were, in turn, housed in modular palm segments that were each independently sensed and controlled. This design decision allowed for easy reconfiguration of the fingers into different arrangements, or even the addition or subtraction of fingers based on application. A promising area of development is implementing actuation to change finger orientation dynamically.

Actuation was achieved through the use of high–torque density gear motors (Greartisan DC 12 V 78 rpm, 380:1 gear ratio), which are inexpensive and widely available. Force output was transmitted to 890 N. Dyneema fishing twine (Docooler 1 mm), which was selected for its high strength-to-diameter ratio, as well as low friction coefficients with most surfaces and slight stretch capacity to handle incidental collisions. Custom anchors were 3D-printed to mount the tendons directly to the output shaft of the motors. Adafruit short flex sensors (ADA1070) were used for joint angle proprioception at both the proximal and distal joints. These piezoresistive components only display unidirectional performance, so they needed to be prestressed before installation to be useful for sensing in both the curled and hyperextended conditions. These sensors were connected to a bank of parallel voltage dividers, with analog signals routed to Arduino Mega that was used as a multi-port data acquisition system.

System control infrastructure

The combination of joint sensing and independent tendon actuation described above allows for a wide range of control options, which are discussed in detail in the Supplementary Materials. The control laws were executed in a middle-level ROS node and transmitted downstream as commanded pulse-width modulation values for a bank of motor drivers via another Arduino Mega. Upstream, more custom ROS infrastructure handled synchronization with a UR5 collaborative robot arm and associated motion control libraries as well as a primary state machine node that provided high-level user interface commands to control task selection. The same infrastructure was used for multiphalange load sharing testing and full-hand manipulation testing.

SUPPLEMENTARY MATERIALS

www.science.org/doi/10.1126/scirobotics.abi9773
Texts S1 to S4
Table S1
Figs. S1 and S2
Movies S1 and S2

REFERENCES AND NOTES

1. A. Bicchi, Hands for dexterous manipulation and robust grasping: A difficult road toward simplicity. *IEEE Trans. Rob. Autom.* **16**, 652–662 (2000).
2. R. R. Ma, A. M. Dollar, On dexterity and dexterous manipulation, in *2011 15th International Conference on Advanced Robotics (ICAR)* (IEEE, 2011).
3. J. N. Israelachvili, *Intermolecular and Surface Forces* (Academic Press, 2015).
4. K. Autumn, Y. A. Liang, S. T. Hsieh, W. Zesch, W. P. Chan, T. W. Kenny, R. Fearing, R. J. Full, Adhesive force of a single gecko foot-hair. *Nature* **405**, 681–685 (2000).
5. Y. Li, J. Krahn, C. Menon, Bioinspired dry adhesive materials and their application in robotics: A review. *J. Bionic Eng.* **13**, 181–199 (2016).
6. E. W. Hawkes, E. V. Eason, A. T. Asbeck, M. R. Cutkosky, The gecko's toe: Scaling directional adhesives for climbing applications. *IEEE ASME Trans. Mechatron.* **18**, 518–526 (2012).
7. A. Asbeck, S. Dastoor, A. Parness, L. Fullerton, N. Esparza, D. Soto, B. Heyneman, M. Cutkosky, Climbing rough vertical surfaces with hierarchical directional adhesion, in *2009 IEEE International Conference on Robotics and Automation* (IEEE, 2009).
8. A. Parness, *Micro-Structured Adhesives for Climbing Applicationjs* (Stanford University, 2010).
9. M. R. Cutkosky, Climbing with adhesion: From bioinspiration to biounderstanding. *Interface Focus* **5**, 20150015 (2015).
10. E. W. Hawkes, E. V. Eason, D. L. Christensen, M. R. Cutkosky, Human climbing with efficiently scaled gecko-inspired dry adhesives. *J. R. Soc. Interface* **12**, 20140675 (2015).
11. J.-P. Roberge, W. Ruotolo, V. Duchaine, M. Cutkosky, Improving industrial grippers with adhesion-controlled friction. *IEEE Robot. Autom. Lett.* **3**, 1041–1048 (2018).
12. P. Glick, S. A. Suresh, D. Ruffatto, M. Cutkosky, M. T. Tolley, A. Parness, A soft robotic gripper with gecko-inspired adhesive. *IEEE Robot. Autom. Lett.* **3**, 903–910 (2018).
13. H. Jiang, E. W. Hawkes, C. Fuller, M. A. Estrada, S. A. Suresh, N. Abcouwer, A. K. Han, S. Wang, C. J. Ploch, A. Parness, M. R. Cutkosky, A robotic device using gecko-inspired adhesives can grasp and manipulate large objects in microgravity. *Sci. Robot.* **2**, eaan4545 (2017).
14. V. Alizadehyazdi, M. Bonthron, M. Spenko, An electrostatic/gecko-inspired adhesives soft robotic gripper. *IEEE Robot. Autom. Lett.* **5**, 4679–4686 (2020).
15. E. W. Hawkes, D. L. Christensen, A. K. Han, H. Jiang, M. R. Cutkosky, Grasping without squeezing: Shear adhesion gripper with fibrillar thin film, in *2015 IEEE International Conference on Robotics and Automation (ICRA)* (IEEE, 2015).
16. G. J. Monkman, An analysis of astrictive prehension. *Int. J. Robot. Res.* **16**, 1–10 (1997).
17. S. Song, C. Majidi, M. Sitti, Geckogripper: A soft, inflatable robotic gripper using geckoinspired elastomer micro-fiber adhesives, in *2014 IEEE/RSJ International Conference on Intelligent Robots and Systems* (IEEE, 2014), pp. 4624–4629.
18. S. Song, D.-M. Drotlef, C. Majidi, M. Sitti, Controllable load sharing for soft adhesive interfaces on three-dimensional surfaces. *Proc. Natl. Acad. Sci. U.S.A.* **114**, E4344–E4353 (2017).
19. J. Hashizume, T. M. Huh, S. A. Suresh, M. R. Cutkosky, Capacitive sensing for a gripper with gecko-inspired adhesive film. *IEEE Robot. Autom. Lett.* **4**, 677–683 (2019).
20. D. Hirano, N. Tanishima, A. Bylard, T. G. Chen, Underactuated gecko adhesive gripper for simple and versatile grasp, in *2020 IEEE International Conference on Robotics and Automation (ICRA)* (IEEE, 2020).
21. P. Day, E. V. Eason, N. Esparza, D. Christensen, M. Cutkosky, Microwedge machining for the manufacture of directional dry adhesives. *J. Micro Nano-Manuf.* **1**, 011001 (2013).
22. S. Wang, H. Jiang, T. Myung Huh, D. Sun, W. Ruotolo, M. Miller, W. R. T. Roderick, H. S. Stuart, M. R. Cutkosky, Spinyhand: Contact load sharing for a human-scale climbing robot. *J. Mech. Robot.* **11**, 031009 (2019).
23. A. Cauligi, Tony G. Chen, S. A. Suresh, M. Dille, R. G. Ruiz, A. M. Vargas, M. Pavone, M. R. Cutkosky, Design and development of a gecko-adhesive gripper for the astrobee free-flying robot. arXiv:2009.09151 [cs.RO] (19 September 2020).
24. W. Ruotolo, F. S. Roig, M. R. Cutkosky, Load-sharing in soft and spiny paws for a large climbing robot. *IEEE Robot. Autom. Lett.* **4**, 1439–1446 (2019).
25. J. Y. Han, Low-cost multi-touch sensing through frustrated total internal reflection, in *UIST '05: Proceedings of the 18th Annual ACM Symposium on User Interface Software and Technology* (ACM, 2005), pp. 115–118.
26. J. K. Salisbury, B. Roth, Kinematic and force analysis of articulated mechanical hands. *J. Mech. Des.* **105**, 35–41 (1983).
27. M. T. Mason, J. K. Salisbury, *Robot Hands and the Mechanics of Manipulation* (The MIT Press, 1985).
28. M. R. Cutkosky, R. D. Howe, Human grasp choice and robotic grasp analysis, in *Dextrous Robot Hands* (Springer, 1990), pp. 5–31.
29. C. Ferrari, J. F. Canny, Planning optimal grasps, in *Proceedings of 1992 IEEE International Conference on Robotics and Automation* (IEEE, 1992).
30. J. Falco, K. Van Wyk, E. Messina, "Performance metrics and test methods for robotic hands" (DRAFT NIST Special Publication 1227, National Institute of Standards and Technology, 2018).
31. J. Bohg, A. Morales, T. Asfour, D. Kragic, Data-driven grasp synthesis—A survey. *IEEE Trans. Robot.* **30**, 289 (2014).

32. E. W. Hawkes, H. Jiang, M. R. Cutkosky, Three-dimensional dynamic surface grasping with dry adhesion. *Int. J. Robot. Res.* **35**, 943–958 (2016).
33. E. V. Eason, E. W. Hawkes, M. Windheim, D. L. Christensen, T. Libby, M. R. Cutkosky, Stress distribution and contact area measurements of a gecko toe using a high-resolution tactile sensor. *Bioinspir. Biomim.* **10**, 016013 (2015).
34. M. Sitti, R. S. Fearing, Synthetic gecko foot-hair micro/nano-structures as dry adhesives. *J. Adhes. Sci. Technol.* **17**, 1055–1073 (2003).
35. K. Autumn, A. Dittmore, D. Santos, M. Spenko, M. Cutkosky, Frictional adhesion: A new angle on gecko attachment. *J. Exp. Biol.* **209**, 3569–3579 (2006).
36. C. Kerst, S. A. Suresh, M. Ferro, M. Cutkosky, Pedot: Pss coating improves gecko-inspired adhesive performance. *J. Micro Nano Manuf.* **8**, 034501 (2020).
37. A. K. Han, A. Hajj-Ahmad, M. R. Cutkosky, Hybrid electrostatic and gecko-inspired gripping pads for manipulating bulky, non-smooth items. *Smart Mater. Struct.* **30**, 025010 (2021).
38. D. A. Dillard, B. Mukherjee, P. Karnal, R. C. Batra, J. Frechette, A review of winkler's foundation and its profound influence on adhesion and soft matter applications. *Soft Matter* **14**, 3669–3683 (2018).
39. M. Ciocarlie, C. Lackner, P. Allen, Soft finger model with adaptive contact geometry for grasping and manipulation tasks, in *Second Joint EuroHaptics Conference and Symposium on Haptic Interfaces for Virtual Environment and Teleoperator Systems (WHC'07)* (IEEE, 2007), pp. 219–224.
40. S. A. A. Moosavian, K. Alipour, On the dynamic tip-over stability of wheeled mobile manipulators. *Int. J. Robot. Autom.* **22**, 322–328 (2007).
41. E. Papadopoulos, D. A. Rey, A new measure of tipover stability margin for mobile manipulators, in *Proceedings of IEEE International Conference on Robotics and Automation* (IEEE, 1996).
42. M. R. Cutkosky, On grasp choice, grasp models, and the design of hands for manufacturing tasks. *IEEE Trans. Robot. Autom.* **5**, 269–279 (1989).
43. G. A. Kragten, M. Baril, C. Gosselin, J. L. Herder, Stable precision grasps by underactuated grippers. *IEEE Trans. Robot.* **27**, 1056–1066 (2011).
44. T. Laliberte, L. Birglen, C. Gosselin, Underactuation in robotic grasping hands. *Mach. Intell. Robot. Control* **4**, 77–87 (2002).
45. Z. Zyada, Y. Hayakawa, S. Hosose, Kinematic analysis of a two-link object for whole arm manipulation, in *ISPRA'10: Proceedings of the 9th WSEAS International Conference on Signal Processing, Robotics and Automation* (ACM, 2010), pp. 139–145.
46. R. M. Murray, Z. Li, S. S. Sastry, S. S. Sastry, *A Mathematical Introduction to Robotic Manipulation* (CRC Press, 1994).
47. D. Prattichizzo, J. K. Salisbury, A. Bicchi, Contact and grasp robustness measures: Analysis and experiments, in *Experimental Robotics IV* (Springer, 1997), pp. 83–90.
48. M. R. Cutkosky, P. K. Wright, Friction, stability and the design of robotic fingers. *Int. J. Robot. Res.* **5**, 20–37 (1986).
49. W. Ruotolo, R. Thomasson, J. Herrera, A. Gruebele, M. Cutkosky, Distal hyperextension is handy: High range of motion in cluttered environments. *IEEE Robot. Autom. Lett.* **5**, 921–928 (2020).
50. W. Wang, S.-H. Ahn, Shape memory alloy-based soft gripper with variable stiffness for compliant and effective grasping. *Soft Robot.* **4**, 379–389 (2017).
51. M. R. Cutkosky, I. Kao, Computing and controlling compliance of a robotic hand. *IEEE Trans. Robot. Autom.* **5**, 151–165 (1989).
52. S. Hirose, Y. Umetani, The development of soft gripper for the versatile robot hand. *Mech. Mach. Theory* **13**, 351–359 (1978).
53. D. M. Aukes, M. R. Cutkosky, Simulation-based tools for evaluating underactuated hand designs, in *2013 IEEE International Conference on Robotics and Automation* (IEEE, 2013).
54. D. M. Aukes, B. Heyneman, J. Ulmen, H. Stuart, M. R. Cutkosky, S. Kim, P. Garcia, A. Edsinger, Design and testing of a selectively compliant underactuated hand. *Int. J. Robot. Res.* **33**, 721–735 (2014).
55. G. A. Kragten, J. L. Herder, The ability of underactuated hands to grasp and hold objects. *Mech. Mach. Theory* **45**, 408–425 (2010).
56. L. U. Odhner, L. P. Jentoft, M. R. Claffee, N. Corson, Y. Tenzer, R. R. Ma, M. Buehler, R. Kohout, R. D. Howe, A. M. Dollar, A compliant, underactuated hand for robust manipulation. *Int. J. Robot. Res.* **33**, 736–752 (2014).
57. B. Soltannia, D. Sameoto, Strong, reversible underwater adhesion via gecko-inspired hydrophobic fibers. *ACS Appl. Mater. Interfaces* **6**, 21995–22003 (2014).
58. S. Xia, Y. Chen, J. Tian, J. Shi, C. Geng, H. Zou, M. Liang, Z. Li, Superior low-temperature reversible adhesion based on bio-inspired microfibrillar adhesives fabricated by phenyl containing polydimethylsiloxane elastomers. *Adv. Funct. Mater.* **31**, 2101143 (2021).
59. N. F. Lepora, K. Aquilina, L. Cramphorn, Exploratory tactile servoing with active touch. *IEEE Robot. Autom. Lett.* **2**, 1156–1163 (2017).
60. Q. Li, C. Schurmann, R. Haschke, H. J. Ritter, A control framework for tactile servoing, in *Robotics: Science and Systems* (2013).
61. M. R. Cutkosky, P. S. Day, E. V. Eason, Mold fabrication method for gecko-inspired adhesives. U.S. Patent 9,908,266 (2018).
62. W. Ruotolo, farmHand kinematics analysis. Zenodo (2021); https://zenodo.org/badge/latestdoi/429142560.

Acknowledgments: We thank M. Lin for editing assistance, A. Hajj-Ahmad for fabrication of gecko-inspired adhesives, and T. Chen for both. **Funding:** Toyota Research Institute (TRI) provided funds to support this work, although this article solely reflects the opinions and conclusions of its authors and not TRI or any other Toyota entity. D.B. was supported by the Stanford Graduate Fellowship. **Author contributions:** W.R. designed and built the hand prototype, wrote the control software, and designed and wrote the simulation and modeling code (excluding FEA analysis of rippling). D.B. performed all ANSYS simulation and setup as well as postprocessing of FTIR results. All authors contributed to paper writing, and W.R. and D.B. both participated in the design, fabrication, and usage of the FTIR test setup as well as design and tuning of the compliant adhesive suspensions. **Competing interests:** The authors declare that they have no competing interests. **Data and materials availability:** All data needed to evaluate the conclusions in the paper are present in the paper or the Supplementary Materials. Code used for kinematics analysis is available at (*62*).

Submitted 4 May 2021
Accepted 18 November 2021
Published 15 December 2021
10.1126/scirobotics.abi9773

Science Robotics

From grasping to manipulation with gecko-inspired adhesives on a multifinger gripper

Wilson Ruotolo, Dane Brouwer, and Mark R. Cutkosky

Sci. Robot. **6** (61), eabi9773. DOI: 10.1126/scirobotics.abi9773

Science Robotics (ISSN 2470-9476) is published by the American Association for the Advancement of Science. 1200 New York Avenue NW, Washington, DC 20005. The title *Science Robotics* is a registered trademark of AAAS.